DR. YUCHI LIU (Orcid ID : 0000-0003-3533-1697)

Article type : Full Paper

Myocardial T_1 and T_2 Quantification and Water-Fat Separation Using Cardiac Magnetic Resonance Fingerprinting with Rosette Trajectories at 3T and 1.5T

Yuchi Liu[1,2], Jesse Hamilton[1,2], Brendan Eck[1,3], Mark Griswold[1,4], Nicole Seiberlich[1,2,4]

[1]Department of Biomedical Engineering, Case Western Reserve University, Cleveland, OH, USA

[2]Department of Radiology, University of Michigan, Ann Arbor, MI, USA

[3]Department of Cardiovascular and Metabolic Sciences, Cleveland Clinic Lerner Research Institute, Cleveland, OH, USA

[4]Department of Radiology, University Hospitals Cleveland Medical Center, Cleveland, OH, USA

Running title: *Rosette cMRF*

Word count: *6394*

Funding sources: R01HL094557, R01DK098503, CBET 1553441.

Disclosure of relationship with industry: our group receives research support from Siemens Healthineers (Erlangen, Germany).

*Address correspondence to:
Nicole Seiberlich, Ph.D.,
1150 West Medical Center Drive,
Ann Arbor, MI, 48109

Email: nse@med.umich.edu
Phone: 734-763-1735

Abstract

Purpose: This work aims to develop an approach for simultaneous water-fat separation and myocardial T_1 and T_2 quantification based on the cardiac Magnetic Resonance Fingerprinting (cMRF) framework with rosette trajectories at 3T and 1.5T.

Methods: Two 15-heartbeat cMRF sequences with different rosette trajectories designed for water-fat separation at 3T and 1.5T were implemented. Water T_1 and T_2 maps, water image and fat image were generated with B_0 inhomogeneity correction using a B_0 map derived from the cMRF data themselves. The proposed water-fat separation rosette cMRF approach was validated in the ISMRM/NIST MRI system phantom and water/oil phantoms. It was also applied for myocardial tissue mapping of healthy subjects at both 3T and 1.5T.

Results: Water T_1 and T_2 values measured using rosette cMRF in the ISMRM/NIST phantom agreed well with the reference values. In the water/oil phantom, oil was well suppressed in the water images and vice versa. Rosette cMRF yielded comparable T_1 but 2~3 ms higher T_2 values in the myocardium of healthy subjects than the original spiral cMRF method. Epicardial fat deposition was also clearly shown in the fat images.

Conclusion: Rosette cMRF provides fat images along with myocardial T_1 and T_2 maps with significant fat suppression. This technique may improve visualization of the anatomical structure of the heart by separating water and fat and could provide value in diagnosing cardiac diseases associated with fibrofatty infiltration or epicardial fat accumulation. It also paves the way towards comprehensive myocardial tissue characterization in a single scan.

Keywords: Cardiac MR Fingerprinting; T_1 mapping; T_2 mapping; fat imaging; water-fat separation; rosette trajectory

Introduction

In non-Cartesian MRI, fat signals are a dominant source of off-resonance artifacts. Fat can cause blurring in images collected along non-Cartesian sampling schemes such as spiral and radial instead of simply a spatial shift in the readout direction as in Cartesian MRI. In order to reduce these chemical shift artifacts due to fat, fat suppression techniques can be used to destroy fat signals before acquisition by exploiting the differences in T_1 or chemical shift of water and fat, resulting in dark areas of fat in the image (1). Water excitation techniques can also be used to select water but not fat protons by means of spectral spatial pulses (2). Alternatively, water-fat separation techniques provide fat images in addition to water images by acquiring both water and fat signals, and then separating them with dedicated post-processing algorithms. These techniques typically use multi-echo Dixon methods (3–8) or special data collection trajectories such as rosette (9). Water-fat separation provides valuable information in various clinical applications (10). Especially in the heart, removal of the fat signals can improve visualization of the anatomical structure of the heart and is also important for imaging coronary arteries (11). Fat identification in the myocardium has potential value in diagnosing intramyocardial fat and fibrofatty infiltration, and lipomas (6,8).

In addition to identifying the presence of fat, relaxation time quantification is another important aspect in myocardial tissue characterization. Compared to anatomical images with T_1- and/or T_2-weighted contrast, myocardial T_1 and T_2 maps have been shown to be more sensitive to a variety of pathological tissue changes, including myocardial inflammation, myocarditis, scar, infarcts (12–17), edema (18–20), sarcoidosis (21), and heart transplant rejection (22,23). Therefore, a comprehensive evaluation of the myocardium including T_1 and T_2 quantification as well as water-fat separation in an efficient way is desirable in the clinic.

In the clinical routine, T_1 and T_2 mapping and fat imaging in the myocardium are often performed in separate scans, where each scan is focused on a single tissue property. Recently, joint tissue property measurements in the myocardium have been proposed to assess multiple tissue properties in a single scan, such as joint T_1 and T_2 mapping (24–27), simultaneous T_1 mapping and water-fat separation (28), and simultaneous T_1, T_2 mapping and fat imaging (29). Among various methods providing the potential for multiple tissue property characterization, the Magnetic Resonance Fingerprinting (MRF) framework has shown promise for myocardial mapping (30–32). Previous studies have also explored simultaneous relaxation time quantification and water-fat separation/fat fraction quantification in the skeletal muscle, liver, brain, breast, and heart (33–38) by combining the MRF framework with variable TE or multi-echo acquisition.

The purpose of this work is to develop an efficient approach based on the cardiac MRF (cMRF) framework to provide myocardial T_1 and T_2 map as well as water-fat separation simultaneously in a single scan for comprehensive cardiac tissue characterization. Rosette trajectories were employed in this work for k-space data sampling as well as water-fat separation (9). The fact that rosette trajectories cross the k-space origin multiple times during each readout enables significant suppression of off-resonance components due to the destructive interference of off-resonance signals. Careful design of the rosette trajectory can result in significant suppression of fat signals when data are reconstructed at the water resonance frequency, and vice versa. By embedding the water-fat separation capability into the data collection trajectory, rosette cMRF requires a minimal modification to the original spiral cMRF pulse sequence (32,39) while adding water-fat separation ability with no penalty in acquisition time. B_0 inhomogeneity correction can also be performed using a B_0 map derived from the rosette cMRF data themselves. The proposed method was validated in the ISMRM/NIST MRI system phantom and water/oil phantoms. It was also applied for myocardial tissue mapping in healthy subjects at both 3T and 1.5T.

Methods

Trajectory and Sequence Design

The rosette trajectory has been used for water-fat separation (9,40,41), simultaneous multi-slice imaging (42,43), T_2* mapping (44–46), and spectroscopic imaging (47) due to its spectral selectivity properties since the 1990s. As the trajectory is played out, off-resonance spins accumulate phase, which is determined by the off-resonance frequency and readout timing; on-resonance spins are not associated with a phase term. Note that the rosette trajectory returns to the center of k-space multiple times during the read-out; each time the trajectory crosses the center of k-space, signals at some off-resonance frequencies can destructively interfere due to their phase differences if the timing is set properly. This signal cancellation can lead to a suppression of the signal from these off-resonance spins. Interested readers are referred to these excellent works (9,40–45,47,48) for more details on the spectral properties of rosette trajectories.

In this work, rosette trajectories were designed using the time optimal gradient design software package developed by Vaziri and Lustig (49,50) with the maximum gradient amplitude of 23 mT/m and maximum slew rate of 145 T/m/s for both 3T and 1.5T MRI scanners. The oscillation frequency w_1, rotational frequency w_2, and number of petals in the rosette trajectories were designed according to the following criteria: FOV 300×300 mm^2, matrix size 192×192, in-plane resolution 1.56×1.56 mm^2, and effective fat suppression at 3T or 1.5T. Two types of rosette trajectories can be generated by using different w_1 and w_2 values ($w_1 > w_2$for Class I; $w_1 < w_2$ for Class II), where w_1 determines the sampling density along the trajectory and w_2 determines the shape of the petal (48). The off-resonance suppression behavior of the trajectory is primarily determined by the shape of the petals and readout duration (a longer readout duration corresponds to more narrowly spaced “null bands” in the spectral domain) (40). In this proof-of-concept work, a fixed value of w_1 with varied w_2 values and readout durations were used to generate multiple Class I and Class II candidate trajectories. To evaluate their spectral responses, simulation studies were performed on a numerical circular phantom by sweeping the off-resonance frequency from 0 to 500 Hz with a step size of 5 Hz and measuring the corresponding signal intensities in the phantom. At 3T, a Class II rosette trajectory (denoted as Rosette A) with four zero-crossings, $w_1 = 0.676\pi\, rad/s$ and $w_2 = 1.01\pi\, rad/s$ (Figure 1a) was used to suppress fat at ~-440Hz; at 1.5T, a Class II rosette trajectory (denoted as Rosette B) with five zero-crossings, $w_1 = 0.676\pi\, rad/s$ and $w_2 = 1.2\pi\, rad/s$ (Figure 1b) was used to suppress fat at ~-220Hz (48).

The pulse sequence used in this study was the previously reported 15-heartbeat, 5-segment scheme ECG-triggered cMRF sequence (39,51) based on the FISP MRF sequence (31).

The five segments are organized with an inversion pulse in the first heartbeat with an inversion time of 21 ms and T_2-preparation pulses in the third, fourth, and fifth heartbeats in each segment with echo times of 30 ms, 50 ms, and 80 ms. No magnetization preparation pulse is used in the second heartbeat. This scheme was repeated three times, resulting in an acquisition over 15-heartbeats during a breath-hold. In the original 15-heartbeat cMRF sequence using the spiral trajectory (51), a fat saturation module was also played out before acquisition in every heartbeat. In the current study, in order to achieve water-fat separation in addition to T_1 and T_2 quantification, the fat saturation module was turned off and the original spiral readout was replaced by Rosette A or Rosette B. The acquisition window in each heartbeat was nearly the same length (~250 ms) at end-diastole. The pulse sequence parameters, including a constant TR and TE, and number of excitations per heartbeat for Rosette A and Rosette B, are summarized in Table 1. The rosette interleaf was rotated by the golden angle (111°) between TRs. Ramped flip angles between 4° to 25°, a slice thickness of 8mm, and in-plane resolution of $1.56 \times 1.56\ \text{mm}^2$ were employed in all phantom and in vivo experiments at both 3T and 1.5T. All data were acquired at the resonance frequency of water.

Image Reconstruction

A schematic showing the overall reconstruction pipeline is shown in Figure 2. Similar to the original cMRF method (32), data acquired in each TR were reconstructed to generate a highly undersampled image using the non-uniform Fast Fourier Transform (NUFFT) (52), leading to a series of 510 or 390 aliased images over 15 heartbeats for the Rosette A and B sequences, respectively. To further reduce aliasing artifacts originating from structures outside the FOV, all in vivo image reconstructions also employed an adaptive coil combination approach with the coil covariance calculated from regions outside the fully-sampled FOV (53,54). Because data were collected at the resonance frequency of water, no additional phase term was added to the k-space data to produce the initial water images in Step 1 (Figure 2). To generate the fat images, the acquired data were shifted to the fat resonance frequency (in other words, demodulated at the resonance frequency of fat) by multiplication of a phase term incorporating the readout duration and fat resonance frequency, as shown in Eq [1]:

$$I_f = F(k_w .* conj(\exp(i2\pi tf))) \quad [1]$$

Here I_f is the fat image, F denotes the operator transforming non-Cartesian k-space data to the image domain, k_w is acquired k-space data with water on-resonance, t is an array of sampling time corresponding to each point of the readout in k_w, and f is the resonance frequency of fat. A single lipid peak was assumed for this work. For different steps of the reconstruction as shown in Figure 2, the resonance frequency of fat used for Eq. [1] was either the theoretical frequency (-440Hz at 3T and -220Hz at 1.5T) or that obtained from the shimming procedure by identifying the peak in the frequency spectrum closest to the theoretical frequency. Details are explained in the following sections.

Dictionary Generation and Pattern Matching

Two separate signal dictionaries, one for water and one for fat, including slice profile and preparation pulse efficiency corrections, were generated as reported previously (55). Subject-specific sequence timing due to variations in heart rate was also taken into account in the dictionary (32). For the water image series, the dictionary resolution, denoted by min:step:max, was [10:10:2000, 2020:20:3000] ms for T_1 in the heart; [10:10:90, 100:20:1000, 1040:40:2000, 2050:100:3000] ms for T_1 in phantoms; [2:2:100, 105:5:200, 210:10:300, 320:20:500] ms for T_2 in the heart; [2:2:8, 10:5:100, 110:10:300, 350:50:1000] ms for T_2 in phantoms. For the fat image series both in the heart and in phantoms, fat signals are assumed to be on-resonance and the dictionary was reduced to [200:10:500] ms for T_1 and [40:2:100] ms for T_2 considering that fat is known to have a T_1 of 360~450ms and T_2 of 48~53ms at 3T, and T_1 of 300~370 and T_2 of ~53 at 1.5T (56,57). Direct pattern matching was used in this work by calculating the inner products between the acquired signal time course at each pixel and the dictionary entries. Both were compressed using the singular value decomposition (SVD) along the time dimension (58). The first six singular values that were greater than 2% of the first (maximum) singular value were retained, and used for pattern matching. The T_1 and T_2 values associated with the dictionary entry that yielded largest inner product were assigned to the pixel to generate the T_1 and T_2 maps, and the scaling factor between the acquired signal time course and the dictionary entry was assigned to the pixel to form the proton density image whose signal intensities were normalized and displayed to the range of [0 1]. In Step 1 (Figure 2), an initial fat image series was reconstructed using the fat frequency obtained from the shimming procedure for Eq. [1], and an initial fat proton density image was produced by matching the fat image series to the fat dictionary.

B_0 Map Calculation

A B_0 map was also derived from the rosette cMRF data. Every two petals of the rosette trajectory were grouped together to form one echo (petals 1 and 2 for echo 1; petals 3 and 4 for echo 2; petal 5 in Rosette B was not used). Each echo consists of approximately the same number of readout points, and the spacing between the two echoes is equal to the readout duration of two petals (ΔTE = 2.81 ms and 3.18 ms for Rosette A and Rosette B, where the time to acquire the first zero-crossing point in the petals is defined as the TE). These two echoes yield two images with different echo times for each TR and thus two image series over the entire 15-heartbeat scan. To reduce aliasing artifacts arising from the highly undersampled images, SVD was performed along the time dimension of these two image series (58,59) and the first coefficient images from each echo was used to calculate the phase difference and therefore the B_0 map according to Eq [2] (60).

$$B_0 = angle(I_{echo1}^{*} I_{echo2})/2\pi\Delta TE \qquad [2]$$

Here I_{echo1}^{*} is the complex conjugate of I_{echo1}. I_{echo1} and I_{echo2} are the images resulting from two echoes, respectively, and ΔTE is the spacing between the two echoes. Because the bandwidth of the B_0 map for Rosette A and B is 1/ ΔTE = 356 and 314 Hz, respectively, which is not sufficient to cover both water and fat (especially at 3T), the process described above was performed on water images and fat images separately to generate two B_0 maps with water and fat on-resonance, respectively. Doubled bandwidth could be achieved with one petal as one echo; however, the images would suffer from severe aliasing artifacts due to limited number of sampling points in one petal. Therefore, two petals were used for each echo in this work to achieve the balance between image quality and B_0 map bandwidth. The theoretical fat resonance frequency was used for Eq. [1] in this step to generate the fat images and fat B_0 map. This approach is based on the assumption that each voxel is either water- or fat-dominant such that the phase difference between the two echoes is only due to B_0 inhomogeneity. A mask obtained from the initial fat proton density image was used to select fat-dominant pixels and combine the two B_0 maps to form a final composite B_0 map. Figure 3a-h shows a schematic of the B_0 mapping process.

B_0 Correction

Following the B_0 map calculation, a frequency-segmented approach was employed for B_0 correction (Step 2 in Figure 2). According to the B_0 inhomogeneity range obtained from the rosette-based B_0 map, a range of demodulating frequencies with a step size of 5Hz was determined for each scan (-200Hz ~ 200Hz was found to be sufficient for in vivo scans). To generate B_0 corrected water images, the acquired data were demodulated at each frequency within the B_0 map range, resulting in a set of images $I_{f(i)}$ with each set demodulated at a frequency f. In each image set I_f, the pixels whose true resonance frequency was close to the demodulating frequency f were assigned to form the final B_0 corrected images. Similarly, to generate B_0 corrected fat images, the acquired data were demodulated at the frequencies which are the sum of the theoretical fat resonance frequency and the B_0 values. Then the same process as described above for water signals was performed. In Step 3 (Figure 2), the B_0-corrected water and fat image series and the water and fat dictionaries were used to generate T_1 maps, T_2 maps, proton density images for both water and fat using pattern matching as described in the previous section. Note that B_0 correction was only implemented for rosette data in both phantom and in vivo experiments but not spiral acquisitions in this work.

Phantom Experiments

To validate the B_0 mapping approach proposed in this work, the B_0 map in a water/oil phantom generated from the rosette cMRF dataset was compared with the GRE B_0 map on a 3T scanner (Siemens MAGNETOM Skyra, Erlangen, Germany). The water/oil phantom contained 10 vials of water doped with Gadolinium (MultiHance, Bracco Inc, NJ, US) and 1 vial of peanut oil (Kraft Heinz, IL, US). The GRE sequence was used to acquire images at two TEs with the following parameters: FOV 300×300 mm^2, matrix size 192×192, slice thickness 8mm, TR 500 ms, TE 7.1 and 14.2 ms. With an echo time difference of 7.1ms, both water and fat are in-phase on the MRI scanner (with a true field strength of ~2.89T), and thus a B_0 map could be generated for both water and fat compartments without a confounding fat chemical shift. The rosette cMRF scan was performed with the same FOV, matrix size, and slice thickness. Note that this rosette cMRF dataset were demodulated at the true fat frequency (~-420Hz on this scanner) to generate the fat B_0 map to enable a comparison with the GRE B_0 map. The maximum, minimum, and averaged differences in B_0 values in the vials were calculated. Differences in B_0 values in the vials were also compared using a linear regression test.

The accuracy of rosette cMRF for water T_1 and T_2 quantification was validated in the ISMRM/NIST MRI system phantom (61,62). The mean and standard deviation of the T_1 and T_2 values in the T_2 layer within physiological range were measured using rosette cMRF and compared with manufacturer provided reference values using a linear regression test. Moreover, to evaluate the difference between B_0 correction using rosette-based and GRE B_0 maps, an external B_0 map was acquired using the two echo GRE sequence as described above at 3T. T_1 and T_2 values before B_0 correction, after B_0 correction using rosette B_0 map and GRE B_0 map were compared with manufacturer provided reference values using a linear regression test. T_1 and T_2 measurements after B_0 correction using the rosette B_0 map and GRE B_0 map were also compared using paired t-test.

The efficacy of rosette cMRF in water-fat separation was demonstrated in a two-compartment water/oil phantom with one vial of oil and one vial of water taken from the 11 vials water/oil phantom described above. Rosette cMRF was compared with 15-heartbeat spiral cMRF without and with fat saturation by calculating the residual oil (water) signal intensity in the water (oil) proton density image. This phantom and the ISMRM/NIST phantom were both scanned on a 3T MRI scanner (Siemens MAGNETOM Skyra, Erlangen, Germany) and a 1.5T scanner (Siemens MAGNETOM Aera, Erlangen, Germany). All phantoms were scanned in an axial orientation with an 18-channel head coil with simulated ECG signals at 60 bpm.

In vivo Experiments

Eleven and five healthy subjects were scanned after written informed consent in this IRB-approved study on a 3T scanner (Siemens MAGNETOM Skyra, Erlangen, Germany) and a 1.5T scanner (Siemens MAGNETOM Aera, Erlangen, Germany), respectively. Mid-ventricular level short axis slices in the heart were acquired using the proposed rosette cMRF sequence and the original spiral 15-heartbeat cMRF sequence with fat saturation. Conventional T_1 and T_2 mapping methods (MOLLI and T_2-prepared FLASH on 3T; MOLLI and T_2-prepared balanced SSFP on 1.5T) were also applied with the same FOV and matrix size as cMRF scans for comparison. The conventional scans are part of the Siemens MyoMaps product and used the following parameters: GRAPPA R=2 and 6/8 Partial Fourier acquisition. The 5(3)3 version of MOLLI was used with an acquisition window of 277 ms. The conventional T_2 mapping scan used a 1(3)1(3)1 acquisition scheme with T_2 preparation times of 0, 25, 55ms and an acquisition window of 228 ms. Shimming was performed over the volume of the heart. In one subject at 3T, the conventional T_1 mapping results were not available due to poor image quality for the MOLLI acquisition, and the conventional T_2 mapping scan was not performed due to limited scan time. ROIs over the entire myocardial wall were drawn manually, and the mean and standard deviation in T_1 and T_2 values were calculated. A student's t-test was used to compare T_1 and T_2 measurements using rosette cMRF, spiral cMRF, and conventional T_1/T_2 mapping sequences. Significant difference was considered with $P<0.05$.

Results

Simulation Data

The spectral responses of the two trajectories used in this study, namely Rosette A and Rosette B, obtained from simulation studies are shown in Figure 1c. The residual signal intensity as compared to the on-resonance signal intensity in the numerical phantom is 4.9% at -440Hz for Rosette A and 13.5% at -220Hz for Rosette B.

Phantom Data

Figure 3 shows images at various steps in the rosette-based B_0 map calculation; the maps generated using the rosette data and GRE acquisition are shown in Figure 3h and i, respectively. The residual difference map between these B_0 maps is shown in Figure 3j. The average B_0 difference in all vials between the rosette composite B_0 map and GRE B_0 map was 9.8 Hz, and the maximum and minimum differences were 23 Hz and -14 Hz. Figure 3k shows the scatter plot of rosette B_0 values of 454 pixels in the phantom compared to those resulting from the GRE B_0 map. The slope of best-fit line was 0.94 with 10Hz difference between the two B_0 maps.

Quantitative results of the T_1 and T_2 measurements in the ISMRM/NIST system phantom are shown in Figure 4. T_1 and T_2 measurements using rosette cMRF were in excellent agreement with the reference values for both Rosette A at 3T (slope of best-fit line 0.97/0.96 for T_1/T_2; $R^2>0.99$) and Rosette B at 1.5T (slope of best-fit line 0.98/0.99 for T_1/T_2; $R^2>0.99$)). At 3T, T_1 and T_2 measurements before B_0 correction, and after B_0 correction using either the rosette B_0 map or the GRE B_0 map all agree well with reference values. No significant difference was observed between the B_0 correction results using rosette B_0 map and GRE B_0 map (P=0.07 for T_1; P=0.28 for T_2) with an average of 11.7Hz difference in the B_0 maps (Supporting Information Figure S1).

Figure 5 shows T_1 maps, T_2 maps, and water and oil proton density images in the water/oil phantom. As can be seen in the water images (third column), rosette images at both 1.5 and 3T showed excellent fat suppression at the resonance frequency of water and vice versa. In the proton density images with signal intensities normalized to the range of [0 1], residual oil signals in the water image were 0.05 and 0.04 at 3T and 1.5T, respectively; residual water signals in the oil image were 0.04 and 0.09 at 3T and 1.5T, respectively. In contrast, the residual oil signal in the water image acquired by spiral cMRF with fat saturation were 0.26 and 0.4 at 3T and 1.5T, respectively. The oil signal in the water image acquired by spiral cMRF without fat saturation were 0.69 and 0.8 at 3T and 1.5T, respectively. In addition to suppressing fat signal effectively, the rosette images also reduce the blurring artifacts seen around the fat vial in the spiral images due to the phase accumulation along the spiral readout. Finally, the T_1 and T_2 values of water at both 1.5T and 3T were similar between rosette and spiral acquisitions (Supporting Information Table S1). Note that the values for T_1 and T_2 in the oil areas are inaccurate in all of these approaches as these are meant to be water maps; any values in the oil vials can be disregarded.

Healthy Subjects

Figure 6 shows representative myocardial T_1 and T_2 maps, water images, and fat images of a mid-ventricular slice in the heart acquired using rosette cMRF before and after B_0 correction compared with those acquired using spiral cMRF with fat saturation and conventional methods at 3T. The B_0 map derived from the rosette cMRF dataset is also shown. Note that signal loss in anterior myocardial wall in the water image that was generated without B_0 correction was recovered after B_0 correction (see arrow). In contrast, spiral images without B_0 correction exhibit blurring in the same area (Supporting Information Figure S2 shows zoomed images around the heart). Representative maps and fat/water images collected in a mid-ventricular slice at 1.5T are shown in Figure 7 and the corresponding zoomed maps and images around the heart are shown in Supporting Information Figure S3. Similar to the results at 3T, both epicardial fat and subcutaneous fat were clearly visualized in the fat image, and suppressed in the water images. Residual water signals in the myocardium and blood pool in the fat proton density image were further reduced after B_0 correction from 0.11 to 0.04 (better visualization in Supporting Information Figure S3).

The averaged and individual myocardial T_1 and T_2 values measured by rosette cMRF after B_0 correction, spiral cMRF, and conventional mapping methods are shown in Figure 8 and Figure 9, respectively. At 3T, rosette cMRF yielded comparable myocardial T_1 compared with spiral cMRF (spiral T_1 1341.7±41.6ms vs. rosette T_1 1329.4±35ms) but significantly higher T_2 values (spiral T_2 30.9±2.3ms vs. rosette T_2 33.3±1.5ms, $P<0.01$). Both spiral and rosette cMRF measurements were 125~135 ms higher than the conventional MOLLI T_1 values (1204.5±30.5ms, $P<0.01$) and 5~7 ms lower than the T_2 values measured by T_2-prepared FLASH (38.5±1.4ms, $P<0.01$). At 1.5T, rosette cMRF and spiral cMRF had comparable T_1 measurements (spiral T_1 1030.8±39.2ms vs. rosette T_1 1044±29.7ms) but the rosette trajectory yielded significantly higher T_2 values (spiral T_2 35.4±1.2ms vs. rosette T_2 39±0.8ms, $P<0.01$). Compared with MOLLI, rosette cMRF gave rise to significantly higher T_1 values (MOLLI T_1 995.7.2±18.1ms, $P<0.05$). Spiral cMRF also had higher T_1 values than MOLLI but the difference was not statistically significant ($P=0.1$). Both rosette and spiral cMRF yielded significantly lower T_2 values than the conventional T_2 mapping method (T_2-prepared balanced SSFP T_2 46.6±1.1ms, $P<0.01$).

Discussion

This study demonstrates that water-fat separation can be achieved along with T_1 and T_2 mapping of the water compartment in the heart in a single scan using rosette cMRF. Off-resonance artifacts due to fat signals are significantly reduced in the water T_1 and T_2 maps and images as shown in the water/oil phantom, and a fat image can be obtained from the same scan with no penalty in acquisition time. The intrinsic property of rosette trajectories that they cross the k-space center multiple times in one readout also enables B_0 mapping using the rosette cMRF data themselves, and thus B_0 inhomogeneity correction can be performed with no need for an extra scan. Moreover, rosette cMRF closely resembles the original 2D spiral cMRF sequence structure, where only the k-space sampling trajectory has been altered. This minor change in readout trajectory can be easily adopted by other cMRF approaches such as simultaneous multislice cMRF (59), 3D cMRF (63), cineMRF (64), and motion resolved cMRF (65), easily adding water-fat separation capabilities to their tool kits.

Rosette Trajectory

The rosette trajectories used in this work are only two examples of possible trajectories which could be designed for water-fat separation. While not optimized for B_0 mapping or complete suppression of fat (or water) signals, these rosette trajectories are a proof-of-principle that this approach can be used for water-fat separation along with relaxation time quantification in the MRF framework. These two trajectories provided robust fat suppression and accurate water T_1 and T_2 measurements across our datasets; however, they have not been specifically optimized in terms of sampling efficiency and they are likely not the only ones that can achieve effective water-fat separation. Because there are multiple “null bands” in the spectral response curve, placing any “null band” around the fat frequency would enable effective water-fat separation, resulting in flexible trajectory design to accommodate either long or short TR values with tunable FOVs and spatial resolution for MRF sequences and beyond. Moreover, the water-fat separation property is only determined by the trajectory itself, providing flexibility in acquisition parameters such as the choice of TE and TR. One challenge when using rosette trajectories is achieving satisfactory image quality within relatively short scan times due to the oversampling property of the trajectory in both the central and peripheral areas of k-space compared to spiral trajectories. MRF is known to be able to tolerate high acceleration factors in each time frame by rejecting noise-like artifacts in the pattern matching step. Due to the already long computing time for B_0 correction, the current study only used direct pattern matching to generate tissue property maps and images. A variety of studies have shown that advanced reconstruction approaches such as multiscale (66) and low rank reconstruction (59,67–69) can significantly improve the image quality of MRF data. The quality of the maps generated with rosette cMRF may also be further improved by incorporating these techniques.

T_1 and T_2 Measurements of the Water Compartment

A previous study has reported that including confounding factors correction (i.e. slice profile and preparation pulse efficiency) in the dictionary leads to increase in T_1 and a decrease in T_2 measurements (55). In the current study, myocardial T_1 and T_2 measurements at 3T using spiral and rosette cMRF are comparable with those previously reported spiral cMRF measurements with confounding factors correction (55). The trend that cMRF yields higher T_1 values than MOLLI and lower T_2 values than conventional T_2 mapping methods is also consistent with previous findings (55,59). T_1 and T_2 measurements using rosette cMRF and spiral cMRF are expected to be comparable in healthy subjects whose myocardial fat is minimal, because the general sequence structure including flip angle patterns and magnetization preparation pulse scheme remains the same for both sequences except for the fat suppression property of rosette cMRF. However, spiral and rosette trajectories react differently to some physiological confounding factors such as flow, and it may result in the slight difference in relaxation time quantification observed in this study (10~15 ms difference in T_1 and 2~3 ms difference in T_2). However, except for T_2, these differences were not statistically significant. Moreover, inaccurate T_1 quantification due to fat signal contamination has been reported in the myocardium for different sequences such as MOLLI and SASHA (70). Compared with spiral cMRF, which employs a fat saturation module before acquisition, rosette cMRF achieves more effective fat suppression as shown in the phantom experiments (Figure 5) and eliminates the need for the fat saturation module, making the sequence design more flexible. It is particularly useful when continuous acquisition is desired for the applications such as free-running cMRF (64). The ~250ms acquisition window is relatively long and may result in motion artifacts due to cardiac motion. Reducing the acquisition window is an active research area in cMRF (71) and the rosette approach could potentially benefit from the application of advanced reconstruction schemes such as low rank model-based approaches (59,67–69).

Water-Fat Separation

In addition to T_1 and T_2 quantification, a fat image can be generated from the same dataset, showing clear epicardial fat deposition (Figure 6, 7). The availability of fat images may provide valuable diagnostic information in cardiac diseases such as myocardial fatty infiltration and lipomas (6), and thus rosette cMRF may prove clinically useful for the visualization of epicardial/myocardial fat deposition. Moreover, intrinsically co-registered T_1 and T_2 maps along with the fat image generated from the same dataset enable a comprehensive evaluation of the myocardial tissue for disease diagnosis.

B_0 Correction

Inhomogeneous B_0 field could be problematic for rosette cMRF because the separation of water and fat using rosette trajectories is based on the distinct resonance frequencies of the two species. One important feature of the proposed approach is that a B_0 map is generated from the rosette cMRF data themselves by taking advantage of the multiple zero-crossings of the rosette trajectory. Therefore, B_0 correction can be performed without the need for an external B_0 mapping scan. Improvements in water-fat separation in vivo by performing B_0 correction are shown in Figure 6 and 7. Note that a few voxels in the chest wall (Figure 6) exhibited signal loss after B_0 correction in this case, because shimming was performed only in the heart region and B_0 inhomogeneity in the chest wall area exceeded the bandwidth of the B_0 map. Note that the choice of demodulating frequency for fat f_{fat} (either the theoretical frequency or the true frequency, which depends on the true field strength of the scanner) would not affect the B_0 correction results for fat-dominant pixels using the proposed method. For these pixels, the sum of B_0 and f_{fat} was used to generate the final B_0-corrected fat images. Because the B_0 values are obtained from demodulated fat images, changes in f_{fat} will lead to compensated changes in the resulting B_0 map, thereby producing the same results.

Comparison with Other Water-Fat MRF Approaches

Some pioneer studies have explored extending the MRF framework for fat saturation and/or measurement, and applied these techniques in skeletal muscle, liver, brain, breast, and heart (33–38). Fat fraction quantification/water-fat separation was achieved along with T_1 (33,37), or both T_1 and T_2 mapping (34–36,38) using variable TE (33,36) or multi-echo acquisition (34,35,37,38) within the MRF framework. However, due to the motion of the heart, cMRF data can only be collected in a limited diastolic acquisition window in each heartbeat (~250ms in this work). Moreover, data collection is restricted to the duration of a breath-hold to avoid respiratory motion. Therefore, the MRF methods developed for static organs would require a significantly longer acquisition time if directly applied to the heart, and thus different approaches must be used for cardiac applications.

Some of these MRF-based fat suppression and quantitative approaches (33,34,37) incorporate not only B_0 generation/correction, but also include B_1^+ correction. Because cMRF requires calculation of a new dictionary for each scan due to heart rate variations, the current study does not take B_1^+ correction into account to avoid long computing time and large storage memory by employing relatively low flip angles that have been shown to reduce sensitivity to B_1^+ inhomogeneity (55). However, B_1^+ can be easily added to the dictionary for correction if needed (55).

The rosette trajectory can be viewed essentially as a multi-echo acquisition. Other multi-echo approaches (34,37,38) acquire only one echo in each TR to achieve a short ΔTE for optimized phase difference between water and fat and relatively long readout such as spiral for efficient k-space coverage. In these approaches, the acquisition time increases proportionally with the number of echoes collected. While multiple echoes can be collected in one TR (35), only radial or Cartesian data collection is rapid enough to accommodate these echoes along with the desired short ΔTE. In contrast, the rosette trajectory can be designed to accommodate multiple echoes (either one single petal or multiple petals can be regarded as one echo) in one TR. Moreover, by tuning the shape and sampling density of the petals, the rosette trajectory offers the flexible choice of effective echo times as well as k-space sampling density for each echo.

A water-fat Dixon cMRF approach has also been reported for simultaneous quantification of T_1, T_2, proton density, and fat fraction in the heart at 1.5T (35). Dixon cMRF and rosette cMRF employ similar sequence structures and magnetization preparation schemes (FISP-based, 5-segment, 15-heartbeat). These two approaches also yielded comparable myocardial T_1 and T_2 values in healthy subjects at 1.5T (Dixon cMRF T_1/T_2 1032/42ms vs. rosette cMRF T_1/T_2 1044/39ms). Moreover, both methods found T_1 measurements higher than MOLLI and T_2 measurements lower than conventional T_2 mapping sequences, which is consistent with previous cMRF reports (55,72). Proton density fat fraction (PDFF) quantification was also shown to be possible using the Dixon cMRF, possibly due to the use of a six-peak fat model in the water-fat separation step.

Limitations and Future Directions

Although the current study is focused on water-fat separation, fat quantification would be an appealing future direction. Fat T_1 and T_2 measurements (especially T_2 at 3T) and further PDFF quantification were found to be inaccurate using the proposed approach. As shown in Supporting Information Figure S4, T_2 values in the oil compartment were comparable with literature values at 1.5T (56,57) but underestimated at 3T. PDFF in water/oil emulsion phantoms constructed according to the method described in Hines et al. (73) were overestimated for low PDFF values (Supporting Information Figure S5,6). One possible explanation for this effect is that off-resonance fat protons may not be prepared by the inversion and T_2-preparation pulses as modeled in the dictionary due to limited bandwidth or imperfect spectral profile of the adiabatic preparation pulses (Supporting Information Figure S7). The inaccuracy is more pronounced at 3T because of the larger chemical shift difference between water and fat compared with 1.5T. This issue could be addressed by optimizing the preparation pulses or taking this effect into account in the signal model for fat in future studies. Other possible reasons include the use of a single peak fat model; a multipeak model has been shown to lead to more accurate fat fraction measurements (74). The single peak model may also limit the accuracy in T_1 and T_2 measurements, as well as B_0 mapping, in the water/oil phantom given that peanut oil has multiple peaks. However, a multipeak fat model can be incorporated in rosette cMRF framework in future studies by demodulating the k-space data at different fat frequencies.

Another limitation of this work is the assumption that a voxel is either water-dominant or fat-dominant. Given that unbalanced SSFP (or FISP) framework is relatively insensitive to off-resonance (31), and off-resonance signals are significantly suppressed by the rosette trajectory, all spins are considered on-resonance for dictionary generation including slice profile and preparation pulse efficiency corrections. However, in the cases where a voxel contains a similar amount of both water and fat such as in diabetic patients, this assumption must be further validated and a more advanced model taking into account of both on- and off-resonance spins might be more desirable. For the dual echo B_0 mapping method proposed in this work, it is challenging to separate chemical shift information of multiple species from true main field inhomogeneity, even though the major source of the chemical shift from fat was taken into account. More accurate B_0 mapping may be enabled by using more echoes in future studies.

The current study demonstrates the proposed method in the heart of healthy subjects; however, it also has the potential for imaging other organs such as liver and knee. Further modifications to the sequence such as removing the waiting time between heartbeats and changing the magnetization preparation scheme need to be investigated to adapt it to other applications.

Conclusion

In conclusion, the proposed rosette cMRF approach achieves effective water-fat separation as well as water T_1 and T_2 quantification in the heart in a single scan. This approach may facilitate cardiac disease diagnosis by providing multiple biomarkers (i.e. fat deposition, water T_1 and T_2) and paves the way towards comprehensive myocardial tissue characterization in a single scan. The acquisition and reconstruction framework may also be easily incorporated into other myocardial mapping methods.

Acknowledgements

This work is supported by R01HL094557, R01DK098503, CBET 1553441, and Siemens Healthineers (Erlangen, Germany). The authors would like to thank Dr. Sanjay Rajagopalan for the insightful discussions.

References

1. Bley TA, Wieben O, François CJ, Brittain JH, Reeder SB. Fat and water magnetic resonance imaging. J. Magn. Reson. Imaging 2010;31:4–18. doi: 10.1002/jmri.21895.
2. Meyer CH, Pauly JM, Macovskiand A, Nishimura DG. Simultaneous spatial and spectral selective excitation. Magn. Reson. Med. 1990;15:287–304. doi: 10.1002/mrm.1910150211.
3. Dixon TW. Simple proton spectroscopic imaging. Radiology 1984;153:189–194. doi: 10.1148/radiology.153.1.6089263.
4. Reeder SB, Markl M, Yu H, Hellinger JC, Herfkens RJ, Pelc NJ. Cardiac CINE imaging with IDEAL water-fat separation and steady-state free precession. J. Magn. Reson. Imaging 2005;22:44–52. doi: 10.1002/jmri.20327.
5. Hernando D, Kellman P, Haldar JP, Liang ZP. Robust water/fat separation in the presence of large field inhomogeneities using a graph cut algorithm. Magn. Reson. Med. 2010;63:79–90. doi: 10.1002/mrm.22177.
6. Kellman P, Hernando D, Shah S, Zuehlsdorff S, Jerecic R, Mancini C, Liang Z-P, Arai AE. Multiecho dixon fat and water separation method for detecting fibrofatty infiltration in the myocardium. Magn. Reson. Med. 2008;61:215–221. doi: 10.1002/mrm.21657.
7. Hernando D, Haldar JP, Sutton BP, Ma J, Kellman P, Liang Z-P. Joint estimation of water/fat images and field inhomogeneity map. Magn. Reson. Med. 2008;59:571–580. doi: 10.1002/mrm.21522.
8. Farrelly C, Shah S, Davarpanah A, Keeling AN, Carr JC. ECG-gated multiecho Dixon fat-water separation in cardiac MRI: Advantages over conventional fat-saturated imaging. Am. J. Roentgenol. 2012;199. doi: 10.2214/AJR.11.7759.
9. Noll DC. Multishot rosette trajectories for spectrally selective MR imaging. IEEE Trans. Med.

Imaging. 1997;16:372–7. doi: 10.1109/42.611345.

10. Hu HH, Börnert P, Hernando D, Kellman P, Ma J, Reeder S, Sirlin C. ISMRM workshop on fat-water separation: Insights, applications and progress in MRI. Magn. Reson. Med. 2012;68:378–388. doi: 10.1002/mrm.24369.

11. Manning WJ, Li W, Boyle NG, Edelman RR. Fat-suppressed breath-hold magnetic resonance coronary angiography. Circulation 1993;87:94–104. doi: 10.1161/01.CIR.87.1.94.

12. Bohnen S, Radunski UK, Lund GK, Kandolf R, Stehning C, Schnackenburg B, Adam G, Blankenberg S, Muellerleile K. Performance of T1 and T2 Mapping Cardiovascular Magnetic Resonance to Detect Active Myocarditis in Patients with Recent-Onset Heart Failure. Circ. Cardiovasc. Imaging 2015;8. doi: 10.1161/CIRCIMAGING.114.003073.

13. Puntmann VO, Nagel E. T1 and T2 Mapping in Nonischemic Cardiomyopathies and Agreement With Endomyocardial Biopsy. J. Am. Coll. Cardiol. 2016;68:1923–1924. doi: 10.1016/j.jacc.2016.06.075.

14. Taylor AJ, Salerno M, Dharmakumar R, Jerosch-Herold M. T1 Mapping Basic Techniques and Clinical Applications. JACC Cardiovasc. Imaging 2016;9:67–81. doi: 10.1016/j.jcmg.2015.11.005.

15. Patel AR, Kramer CM. Role of Cardiac Magnetic Resonance in the Diagnosis and Prognosis of Nonischemic Cardiomyopathy. JACC Cardiovasc. Imaging 2017;10:1180–1193. doi: 10.1016/j.jcmg.2017.08.005.

16. Burt JR, Zimmerman SL, Kamel IR, Halushka M, Bluemke DA. Myocardial T1 mapping: techniques and potential applications. Radiographics. 2014;34:377–95. doi: 10.1148/rg.342125121.

17. Hamlin SA, Henry TS, Little BP, Lerakis S, Stillman AE. Mapping the Future of Cardiac MR Imaging: Case-based Review of T1 and T2 Mapping Techniques. RadioGraphics 2014;34:1594–1611. doi: 10.1148/rg.346140030.

18. Verhaert D, Thavendiranathan P, Giri S, Mihai G, Rajagopalan S, Simonetti OP, Raman S V. Direct T2 quantification of myocardial edema in acute ischemic injury. JACC Cardiovasc. Imaging 2011;4:269–278. doi: 10.1016/j.jcmg.2010.09.023.

19. Giri S, Chung Y-C, Merchant A, Mihai G, Rajagopalan S, Raman SV, Simonetti OP. T2 quantification for improved detection of myocardial edema. J. Cardiovasc. Magn. Reson. 2009;11:56. doi: 10.1186/1532-429X-11-56.

20. Park CH, Choi EY, Kwon HM, et al. Quantitative T2 mapping for detecting myocardial edema after reperfusion of myocardial infarction: Validation and comparison with T2-weighted images. Int. J. Cardiovasc. Imaging 2013;29:65–72. doi: 10.1007/s10554-013-0256-0.
21. Crouser ED, Ono C, Tran T, He X, Raman S V. Improved detection of cardiac sarcoidosis using magnetic resonance with myocardial T2 mapping. Am. J. Respir. Crit. Care Med. 2014;189:109–112. doi: 10.1164/rccm.201309-1668LE.
22. Butler CR, Thompson R, Haykowsky M, Toma M, Paterson I. Cardiovascular magnetic resonance in the diagnosis of acute heart transplant rejection: a review. J. Cardiovasc. Magn. Reson. 2009;11:7. doi: 10.1186/1532-429X-11-7.
23. Butler CR, Savu A, Bakal JA, et al. Correlation of cardiovascular magnetic resonance imaging findings and endomyocardial biopsy results in patients undergoing screening for heart transplant rejection. J. Hear. Lung Transplant. Off. Publ. Int. Soc. Hear. Transplant. 2015;34:643–650. doi: 10.1016/j.healun.2014.12.020.
24. Blume U, Lockie T, Stehning C, Sinclair S, Uribe S, Razavi R, Schaeffter T. Interleaved T1 and T2 relaxation time mapping for cardiac applications. J. Magn. Reson. Imaging 2009;29:480–487. doi: 10.1002/jmri.21652.
25. Akçakaya M, Weingärtner S, Basha TA, Roujol S, Bellm S, Nezafat R. Joint myocardial T1 and T2 mapping using a combination of saturation recovery and T2-preparation. Magn. Reson. Med. 2016;76:888–896. doi: 10.1002/mrm.25975.
26. Kvernby S, Warntjes MJB, Haraldsson H, Carlhäll CJ, Engvall J, Ebbers T. Simultaneous three-dimensional myocardial T1 and T2 mapping in one breath hold with 3D-QALAS. J. Cardiovasc. Magn. Reson. 2014;16:102. doi: 10.1186/s12968-014-0102-0.
27. Santini F, Kawel-Boehm N, Greiser A, Bremerich J, Bieri O. Simultaneous T1 and T2 quantification of the myocardium using cardiac balanced-SSFP inversion recovery with interleaved sampling acquisition (CABIRIA). Magn. Reson. Med. 2015;74:365–371. doi: 10.1002/mrm.25402.
28. Nezafat M, Nakamori S, Basha TA, Fahmy AS, Hauser T, Botnar RM. Imaging sequence for joint myocardial T1mapping and fat/water separation. Magn. Reson. Med. 2018:486–494. doi: 10.1002/mrm.27390.
29. Milotta G, Ginami G, Bustin A, Neji R, Prieto C, Botnar R. 3D Whole-heart High-resolution Motion Compensated Joint T1/T2 Mapping. In: Proc Int Soc Mag Reson Med. 27. 2019. p. 2003.

30. Ma D, Gulani V, Seiberlich N, Liu K, Sunshine JL, Duerk JL, Griswold MA. Magnetic resonance fingerprinting. Nature 2013;495:187–92. doi: 10.1038/nature11971.

31. Jiang Y, Ma D, Seiberlich N, Gulani V, Griswold M. MR fingerprinting using fast imaging with steady state precession (FISP) with spiral readout. Magn. Reson. Med. 2015;74:1621–1631. doi: 10.1002/mrm.25559.

32. Hamilton JI, Jiang Y, Chen Y, Ma D, Lo WC, Griswold M, Seiberlich N. MR fingerprinting for rapid quantification of myocardial T1, T2, and proton spin density. Magn. Reson. Med. 2017;77:1446–1458. doi: 10.1002/mrm.26216.

33. Cencini M, Biagi L, Kaggie JD, Schulte RF, Tosetti M, Buonincontri G. Magnetic resonance fingerprinting with dictionary - based fat and water separation (DBFW MRF): A multi - component approach. Magn Reson Med 2019;81:3032–3045. doi: 10.1002/mrm.27628.

34. Koolstra K, Webb A, Koken P, Nehrke K, Börnert P. Water-Fat Separation in Spiral Magnetic Resonance Fingerprinting using Conjugate Phase Reconstruction. In: Proc Int Soc Mag Reson Med. 26. 2018. p. 0681.

35. Jaubert O, Cruz G, Bustin A, et al. Water–fat Dixon cardiac magnetic resonance fingerprinting. Magn. Reson. Med. 2019;00:1–17. doi: 10.1002/mrm.28070.

36. Ostenson J, Damon BM, Welch EB. MR fingerprinting with simultaneous T1, T2, and fat signal fraction estimation with integrated B0 correction reduces bias in water T1 and T2 estimates. Magn. Reson. Imaging 2019;60:7–19. doi: 10.1016/j.mri.2019.03.017.

37. Marty B, Carlier PG. MR fingerprinting for water T1 and fat fraction quantification in fat infiltrated skeletal muscles. Magn. Reson. Med. 2019:mrm.27960. doi: 10.1002/mrm.27960.

38. Nolte T, Gross-Weege N, Doneva M, Koken P, Elevelt A, Truhn D, Kuhl C, Schulz V. Spiral blurring correction with water–fat separation for magnetic resonance fingerprinting in the breast. Magn. Reson. Med. 2020;83:1192–1207. doi: 10.1002/mrm.27994.

39. Liu Y, Hamilton J, Rajagopalan S, Seiberlich N. Cardiac Magnetic Resonance Fingerprinting: Technical Overview and Initial Results. JACC Cardiovasc. Imaging 2018;11:1837:53. doi: 10.1016/j.jcmg.2018.08.028.

40. Schirda C V, Tanase C, Boada FE. Rosette spectroscopic imaging: optimal parameters for alias-free, high sensitivity spectroscopic imaging. J. Magn. Reson. Imaging. 2009;29:1375–85. doi: 10.1002/jmri.21760.

41. Bucholz EK, Song J, Johnson GA, Hancu I. Multispectral imaging with three-dimensional

rosette trajectories. Magn. Reson. Med. 2008;59:581–589. doi: 10.1002/mrm.21551.

42. Peltier SJ, Noll DC. Systematic noise compensation for simultaneous multislice acquisition using rosette trajectories (SMART). Magn. Reson. Med. 1999;41:1073–1076. doi: 10.1002/(SICI)1522-2594(199905)41:5<1073::AID-MRM28>3.0.CO;2-5.

43. Noll DC, Peltier SJ, Boada FE. Simultaneous multislice acquisition using rosette trajectories (SMART): A new imaging method for functional MRI. Magn. Reson. Med. 1998;39:709–716. doi: 10.1002/mrm.1910390507.

44. Twieg DB. Parsing local signal evolution directly from a single-shot MRI signal: a new approach for fMRI. Magn. Reson. Med. 2003;50:1043–52. doi: 10.1002/mrm.10613.

45. Hu C, Reeves S, Peters DC, Twieg D. An Efficient Reconstruction Algorithm Based on the Alternating Direction Method of Multipliers for Joint Estimation of R2∗ and Off-Resonance in fMRI. IEEE Trans. Med. Imaging 2017;36:1326–1336. doi: 10.1109/TMI.2017.2667698.

46. Lee S, Noll D, Fessler JA. EXTended Rosette ACquisition Technique (EXTRACT): a dynamic R2* mapping method using extended rosette trajectory. In: Proc Int Soc Mag Reson Med. 11. 2004. p. 2128.

47. Schirda C V., Zhao T, Andronesi OC, Lee Y, Pan JW, Mountz JM, Hetherington HP, Boada FE. In vivo brain rosette spectroscopic imaging (RSI) with LASER excitation, constant gradient strength readout, and automated LCModel quantification for all voxels. Magn. Reson. Med. 2016;76:380–390. doi: 10.1002/mrm.25896.

48. Li Y, Yang R, Zhang C, Zhang J, Jia S, Zhou Z. Analysis of generalized rosette trajectory for compressed sensing MRI. Am. Assoc. Phys. Med. 2015;42:5530–5544. doi: 10.1118/1.4928152.

49. Lustig M, Kim SJ, Pauly JM. A fast method for designing time-optimal gradient waveforms for arbitrary k-space trajectories. IEEE Trans. Med. Imaging 2008;27:866–873. doi: 10.1109/TMI.2008.922699.

50. Vaziri S, Lustig M. The Fastest Arbitrary k-space Trajectories. In: Proc Intl Soc Mag Reson Med. 20. 2012. p. 2284.

51. Hamilton JI, Jiang Y, Ma D, Pahwa S, Chen Y, Lo W-C, Griswold MA, Seiberlich N. A Comparison of 5-Heartbeat vs. 15-Heartbeat Cardiac MR Fingerprinting Sequences in Normal Volunteers. In: ISMRM workshop on MRF. 2017.

52. Fessler JA, Sutton BP. Nonuniform fast Fourier transforms using min-max interpolation. IEEE Trans. Signal Process. 2003;51:560–574. doi: 10.1109/TSP.2002.807005.

53. Walsh DO, Gmitro AF, Marcellin MW. Adaptive reconstruction of phased array MR imagery. Magn Reson Med 2000;43:682:90. doi: 10.1002/(SICI)1522-2594(200005)43:5<682::AID-MRM10>3.0.CO;2-G.

54. Mandava S, Keerthivasan MB, Martin DR, Altbach MI, Bilgin A. Radial streak artifact reduction using phased array beamforming. Magn. Reson. Med. 2019. doi: 10.1002/mrm.27689.

55. Hamilton JI, Jiang Y, Ma D, Lo W-C, Gulani V, Griswold M, Seiberlich N. Investigating and reducing the effects of confounding factors for robust T1 and T2 mapping with cardiac MR fingerprinting. Magn. Reson. Imaging 2018;53:40–51. doi: 10.1016/j.mri.2018.06.018.

56. Jordan CD, Saranathan M, Bangerter NK, Hargreaves BA, Gold GE. Musculoskeletal MRI at 3.0 T and 7.0 T: A comparison of relaxation times and image contrast. Eur. J. Radiol. 2013;82:734–739. doi: 10.1016/j.ejrad.2011.09.021.

57. Rakow-Penner R, Daniel B, Yu H, Sawyer-Glover A, Glover GH. Relaxation times of breast tissue at 1.5T and 3T measured using IDEAL. J. Magn. Reson. Imaging 2006;23:87–91. doi: 10.1002/jmri.20469.

58. McGivney DF, Pierre E, Ma D, Jiang Y, Saybasili H, Gulani V, Griswold MA. SVD compression for magnetic resonance fingerprinting in the time domain. IEEE Trans. Med. Imaging 2014;33:2311–2322. doi: 10.1109/TMI.2014.2337321.

59. Hamilton JI, Jiang Y, Ma D, Chen Y, Lo W-C, Griswold M, Seiberlich N. Simultaneous multislice cardiac magnetic resonance fingerprinting using low rank reconstruction. NMR Biomed. 2018;32:e4041. doi: 10.1002/nbm.4041.

60. Irarrazabal P, Meyer CH, Nishimura DG, Macovski a. Inhomogeneity correction using an estimated linear field map. Magn. Reson. Med. 1996;35:278–82.

61. Keenan K, Stupic K, Russek S, Chenevert T, Prasad P, Reddick W, Cecil K, Jackson E. Multi-site, multi-vendor comparison of T1 measurement using ISMRM/NIST system phantom. In: Proc Int Soc Mag Reson Med. 24. 2016. p. 3290.

62. Russek S, Boss M, Jackson E, Jennings D, Eveloch J, Gunter J, Sorensen A. Characterization of NIST/ISMRM MRI system phantom. In: Proc Int Soc Mag Reson Med. 20. 2012. p. 2456.

63. Jaubert O, Cruz G, Bustin A, Schneider T, Botnar RM, Prieto C. Toward 3D Free-breathing Cardiac Magnetic Resonance Fingerprinting. In: Proc Intl Soc Mag Reson Med. 27. 2019. p. 4385.

64. Hamilton JI, Griswold M, Seiberlich N. Combined Cardiac CINE and T1, T2, and M0

Mapping with MR Fingerprinting. In: Proc Intl Soc Mag Reson Med. 27. 2019. p. 0405.
65. Jaubert O, Cruz G, Bustin A, Schneider T, Koken P, Doneva M, Botnar RM, Prieto C. Cardiac motion resolved Magnetic Resonance Fingerprinting with joint reconstruction: jMORE-MRF. In: Proc Intl Soc Mag Reson Med. 27. 2019. p. 0808.
66. Pierre EY, Ma D, Chen Y, Badve C, Griswold MA. Multiscale reconstruction for MR fingerprinting. Magn. Reson. Med. 2016;75:2481–2492. doi: 10.1002/mrm.25776.
67. Zhao B, Setsompop K, Adalsteinsson E, Gagoski B, Ye H, Ma D, Jiang Y, Ellen Grant P, Griswold MA, Wald LL. Improved magnetic resonance fingerprinting reconstruction with low-rank and subspace modeling. Magn. Reson. Med. 2018;79:933–942. doi: 10.1002/mrm.26701.
68. Assländer J, Cloos MA, Knoll F, Sodickson DK, Hennig J, Lattanzi R. Low rank alternating direction method of multipliers reconstruction for MR fingerprinting. Magn. Reson. Med. 2018;79:83–96. doi: 10.1002/mrm.26639.
69. Lima da Cruz G, Bustin A, Jaubert O, Schneider T, Botnar RM, Prieto C. Sparsity and locally low rank regularization for MR fingerprinting. Magn. Reson. Med. 2019;81:3530–3543. doi: 10.1002/mrm.27665.
70. Larmour S, Chow K, Kellman P, Thompson RB. Characterization of T1 bias in skeletal muscle from fat in MOLLI and SASHA pulse sequences: Quantitative fat-fraction imaging with T1 mapping. Magn. Reson. Med. 2017;77:237–249. doi: 10.1002/mrm.26113.
71. Eck B, Liu Y, Seiberlich N, Hamilton J. Influence of scan window duration on parameter maps from cardiac magnetic resonance fingerprinting. In: SCMR 22 Annual Scientific Sessions. 2019. p. 325.
72. Hamilton JI, Pahwa S, Adedigba J, et al. Simultaneous Mapping of T1 and T2 Using Cardiac Magnetic Resonance Fingerprinting in a Cohort of Healthy Subjects at 1.5T. J. Magn. Reson. Imaging 2020. doi: 10.1002/jmri.27155.
73. Hines CDG, Yu H, Shimakawa A, McKenzie CA, Brittain JH, Reeder SB. T1 independent, T2* corrected MRI with accurate spectral modeling for quantification of fat: Validation in a fat-water-SPIO phantom. J. Magn. Reson. Imaging 2009;30:1215–1222. doi: 10.1002/jmri.21957.
74. Hernando D, Liang ZP, Kellman P. Chemical shift-based water/fat separation: A comparison of signal models. Magn. Reson. Med. 2010:811–822. doi: 10.1002/mrm.22455.

Table 1. Summary of acquisition parameters of the rosette cMRF sequences and spiral cMRF sequences with fat saturation module on and off at 3T and 1.5T.

Trajectory	Fat Sat Module	Field Strength	TR (ms)	TE (ms)	Excitations /Heartbeat	Acquisition Window/ Heartbeat (ms)	Acquisition Time
Rosette A	off	3T	7.36	1.39	34	250.2	15 heartbeats
Rosette B	off	1.5T	9.7	1.39	26	252.2	
Spiral	on	3T & 1.5T	5.1	1.39	50	255	
Spiral	off						

Figure Legends

Figure 1. Designed rosette trajectories and their spectral responses. One interleaf of Rosette A **(a)** and Rosette B **(b)** are shown with each petal in a different color and their order indicated by numbers. Their spectral responses were evaluated on a numerical phantom in simulation studies by sweeping the off-resonance frequency from 0 to 500 Hz with a step size of 5 Hz **(c)**. Rosette A was designed for fat suppression at -440Hz at 3T as indicated by the blue arrow; Rosette B was designed for fat suppression at -220Hz at 1.5T as indicated by the red arrow.

Figure 2. The reconstruction pipeline. Step 1: B_0 map generation. Every two petals of the rosette trajectory were grouped as one echo (petals 1 and 2 for echo 1; petals 3 and 4 for echo 2. Rosette A is shown here for demonstration) to generate two images at the water frequency or the fat frequency. The first coefficient images ($\boldsymbol{I_{W1}}\ \ \boldsymbol{I_{W2}}\ \boldsymbol{I_{F1}}\ \boldsymbol{I_{F2}}$) from SVD of the water/fat image series at two echo times are used for B_0 map calculation. Then a limited bandwidth B_0 map centered at water or fat frequency was calculated from the two images. A mask from the initial fat image was used to form a final composite B_0 map. **Step 2**: Water and fat image series where one image from each TR was reconstructed with B_0 correction. **Step 3**: Final tissue property maps and proton density images were generated by matching the water or fat image series to the corresponding dictionary.

$\boldsymbol{f_1}$: the theoretical fat frequency (i.e. -440Hz at 3T; -220Hz at 1.5T); $\boldsymbol{f_2}$: the fat frequency obtained from the shimming procedure before the scan started; $\boldsymbol{D_W}$: water dictionary; $\boldsymbol{D_F}$: fat dictionary.

Figure 3. B_0 map in the water/oil phantom generated from the rosette cMRF dataset compared with GRE B_0 map at 3T. (a-d) The first coefficient images from SVD of the water/oil image series at two echo times. **(e-f)** B_0 maps generated by calculating the phase difference between the images at two echo times for water **(a, b)** and oil **(c, d)**, respectively. The bandwidth of each rosette B_0 map here is 356Hz. An initial oil image **(g)** was used as a mask to combine the water and oil B_0 maps and generate the rosette composite B_0 map **(h)**. The GRE B_0 map **(i)** and the residual map between GRE and rosette composite B_0 map **(j)** are also shown. Averaged B_0 difference in all compartments is 9.8 Hz as shown in the residual map **(j)**. **(k)** Scatter plot of rosette B_0 values of 454 pixels in the phantom compared to those resulting from the GRE B_0 map.

Figure 4. Results in the ISMRM/NIST MRI system phantom. The mean and standard deviation of the T_1 and T_2 measurements using rosette cMRF were compared with reference values at 3T **(a)** and 1.5T **(b)**. The maximum standard deviation of T_1 and T_2 measurements at 3T were 35 ms and 4.4 ms; at 1.5T were 48 ms and 7.2 ms, respectively. For T_1 over all vials, the standard deviation was less than 7% of the mean value at both 3T and 1.5T. For T_2 over all vials within the physiological range, the standard deviation was less than 5% of the mean value at both 3T and 1.5T.

Figure 5. Results in the water/oil phantom. Water T_1 maps, T_2 maps and proton density images generated by spiral cMRF without and with fat saturation, and water T_1 maps, T_2 maps, and water and fat proton density images generated using rosette cMRF at 3T (top three rows) and 1.5T (bottom three rows) are shown. A cropped FOV of 100x100 mm^2 is displayed. Signal intensities of the water and oil compartment are labeled in the proton density images. All spiral maps and images are without B_0 correction, and all rosette maps and images are with B_0 correction using the rosette-derived B_0 map.

Figure 6. Results in a healthy subject at 3T. Representative T_1, T_2 maps, water and fat images of a mid-ventricular slice in the heart acquired using rosette cMRF, spiral cMRF with fat saturation, and conventional methods are shown. The B_0 map derived from rosette cMRF dataset

and the results before and after B_0 correction are also shown for comparison. Signal loss in the anterior myocardial wall observed in the water image was recovered after B_0 correction as pointed by the arrow. Epicardial fat and subcutaneous fat was clearly visualized in the fat image, and suppressed in all of the water maps and images. Zoomed images around the heart are available in Supporting Information Figure S2.

Figure 7. Results in a healthy subject at 1.5T. Representative T_1, T_2 maps, water and fat images of a mid-ventricular slice in the heart acquired using rosette cMRF, spiral cMRF with fat saturation, and conventional methods are shown. The B_0 map derived from rosette cMRF dataset and the results before and after B_0 correction are also shown for comparison. Epicardial fat and subcutaneous fat was clearly visualized in the fat image, and suppressed in all of the water maps and images. Residual water signals in the myocardium and blood pool in the fat image (indicated by the arrow) was further reduced by B_0 correction from 0.11 to 0.04. Zoomed images around the heart are available in Supporting Information Figure S3.

Figure 8. Averaged T_1 and T_2 measurements over the entire myocardial wall among 11 healthy subjects at 3T and 5 healthy subjects at 1.5T. Statistical significance was considered with $P<0.05$.

Figure 9. Individual T_1 and T_2 measurements over the entire myocardial wall among 11 healthy subjects at 3T and 5 healthy subjects at 1.5T.

Supporting Information Figure S1. T_1 and T_2 measurements using rosette cMRF in the NIST/ISMRM phantom at 3T. Rosette cMRF measurements before B_0 correction, after B_0 correction using the rosette-based B_0 map, and after correction using the GRE-based B_0 map all agree well with reference values ($R^2>0.99$). The differences in B_0 values in the vials between rosette and GRE B_0 maps range from 5 to 20 Hz, with an average difference of 11.7Hz. No significant difference ($P=0.07$ for T_1; $P=0.28$ for T_2) was found between the B_0 correction results using rosette and GRE B_0 maps.

Supporting Information Figure S2. Zoomed maps and images around the heart in a healthy subject at 3T. Without B_0 correction, off-resonance artifacts in the anterior myocardial wall appear as signal loss in rosette images but blurring in spiral images as indicated by the arrows. The signal loss in rosette images was recovered by B_0 correction.

Supporting Information Figure S3. Zoomed maps and images around the heart in a healthy subject at 1.5T. The color scale of the fat images is set to [0 0.5] instead of [0 1] to enable visualization of the improvement in water-fat separation after B_0 correction.

Supporting Information Figure S4. T_1, T_2 maps and proton density images of both water and oil acquired using rosette cMRF in the water/oil phantom at 3T and 1.5T. The water specific maps and images are the same as those shown in Figure 5. A cropped FOV of 100×100 mm^2 is displayed. At 3T: oil T_1 252.09 ± 7.98 ms; T_2 40 ± 0 ms. At 1.5T: oil T_1 202.43 ± 4.32 ms; T_2 55.51 ± 3.15 ms.

Supporting Information Figure S5. T_1 and T_2 maps, and proton density images of water and fat in an agar-based water/fat mixture phantom at 3T and 1.5T. PDFF maps calculated from the water and fat proton density images are also shown. Designed PDFF of each vial is shown at bottom right.

Supporting Information Figure S6. PDFF values calculated from water and fat proton density images in an agar-based water/fat mixture phantom acquired using rosette cMRF compared with ground truth at 3T and 1.5T.

Supporting Information Figure S7. Bloch simulations of the adiabatic inversion pulse (a) and the 90° adiabatic excitation pulse in the T_2-preparation module (b). Longitudinal magnetization (Mz) after the pulses was evaluated for T_1=1000ms, T_2=100ms over a range of off-resonance frequencies from -500Hz to 500Hz with a step size of 5Hz.

Supporting Information Table S1. T_1 and T_2 values in the water compartment in the water/oil phantom at 3T and 1.5T acquired using rosette cMRF and spiral cMRF.

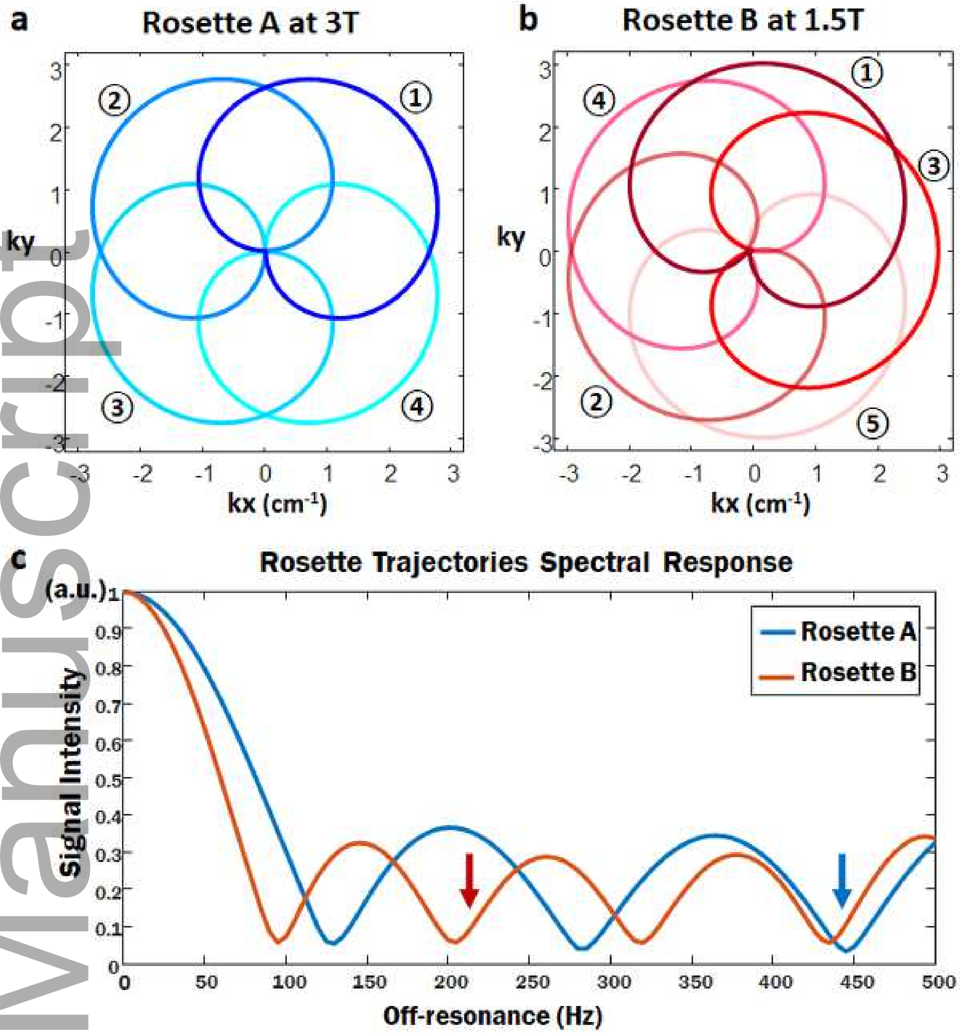

mrm_28404_f1.tif

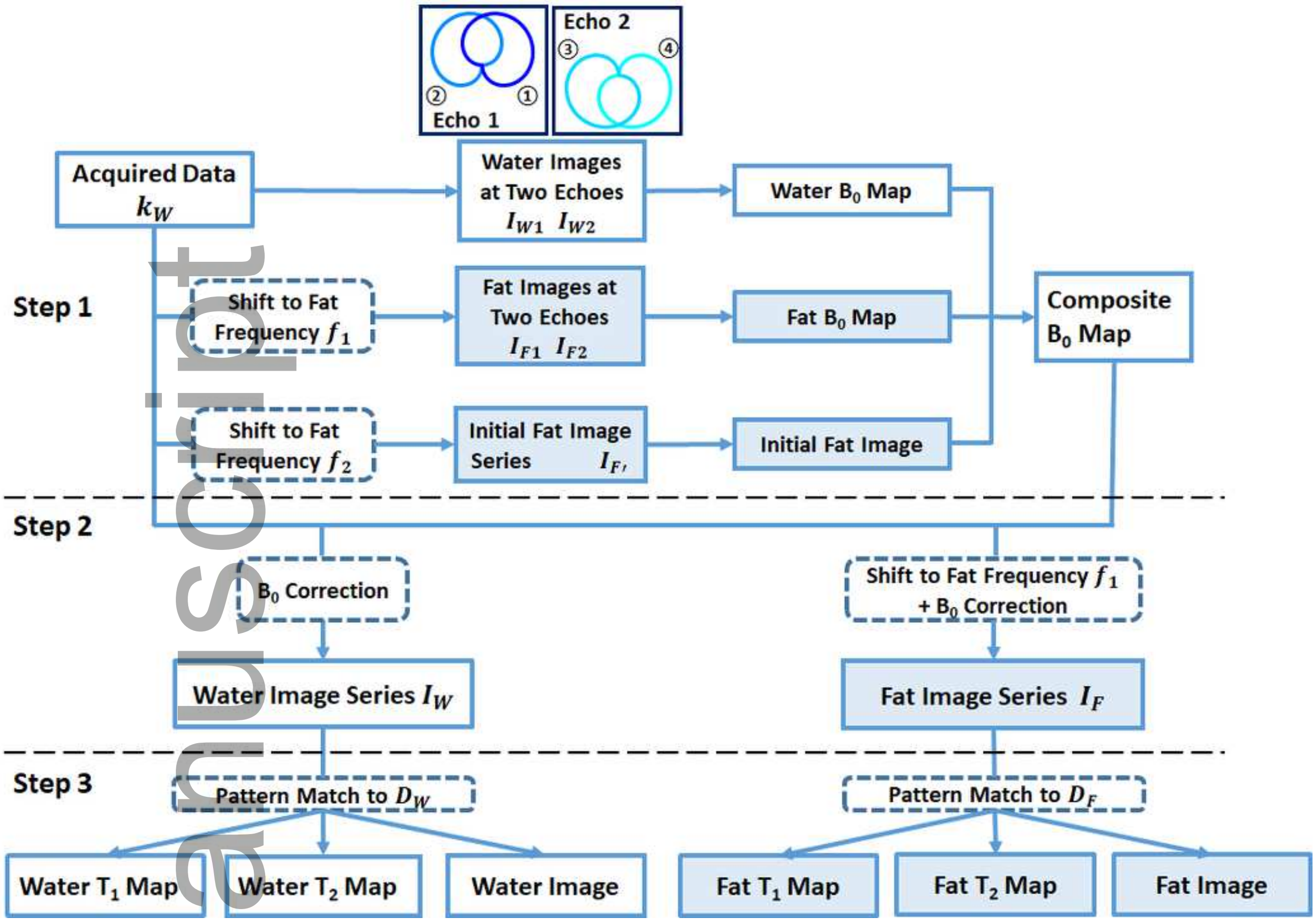

mrm_28404_f2.tif

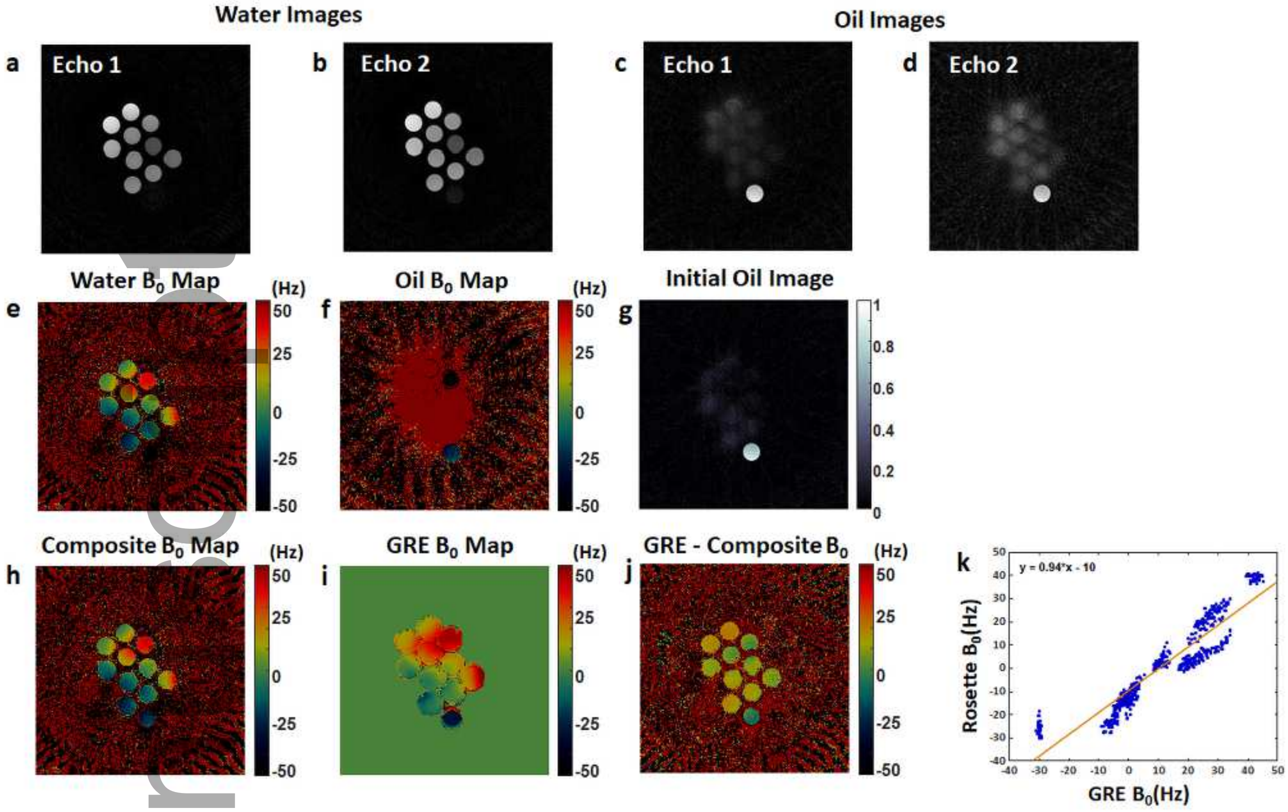

mrm_28404_f3.tif

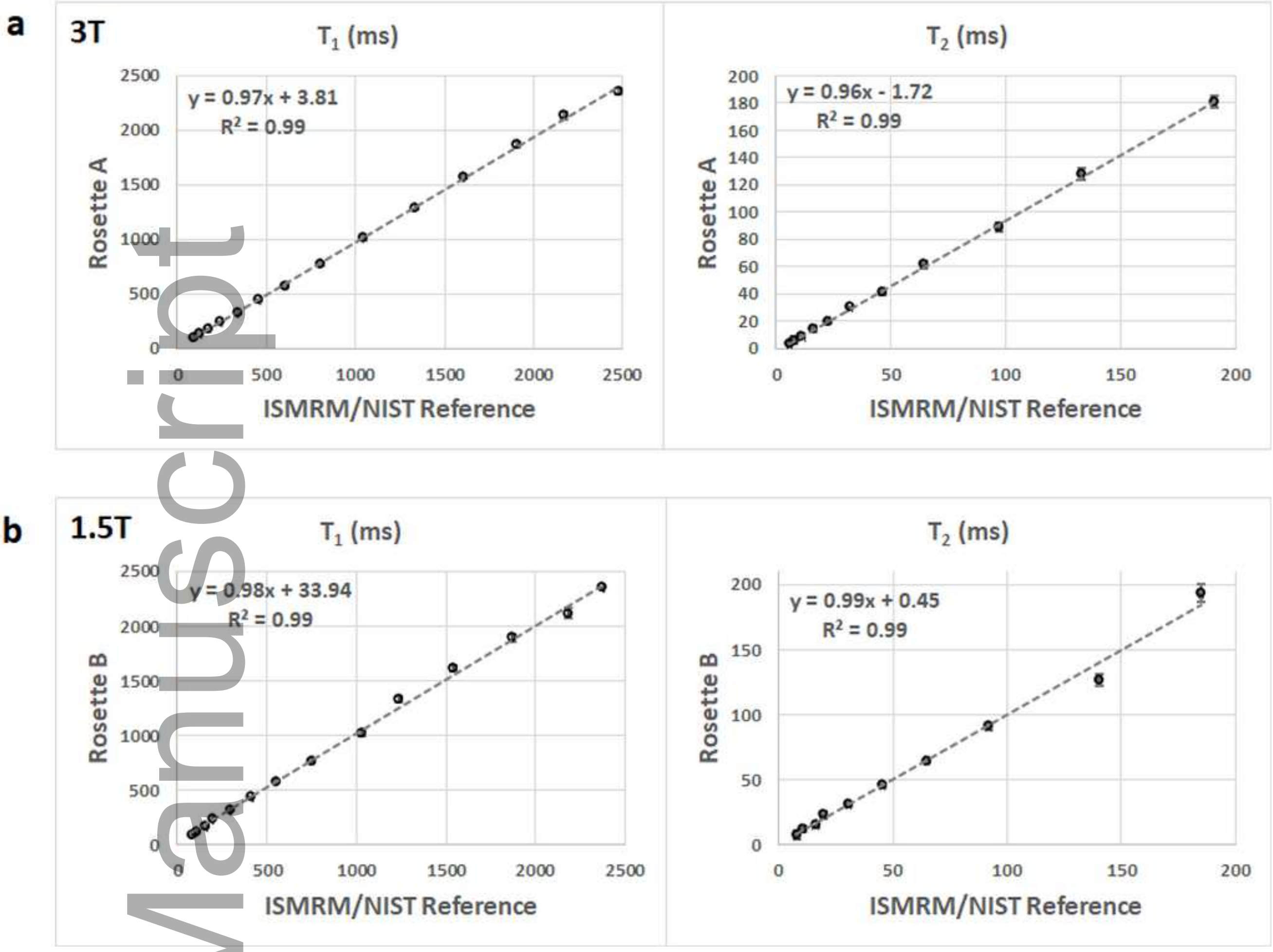

mrm_28404_f4.tif

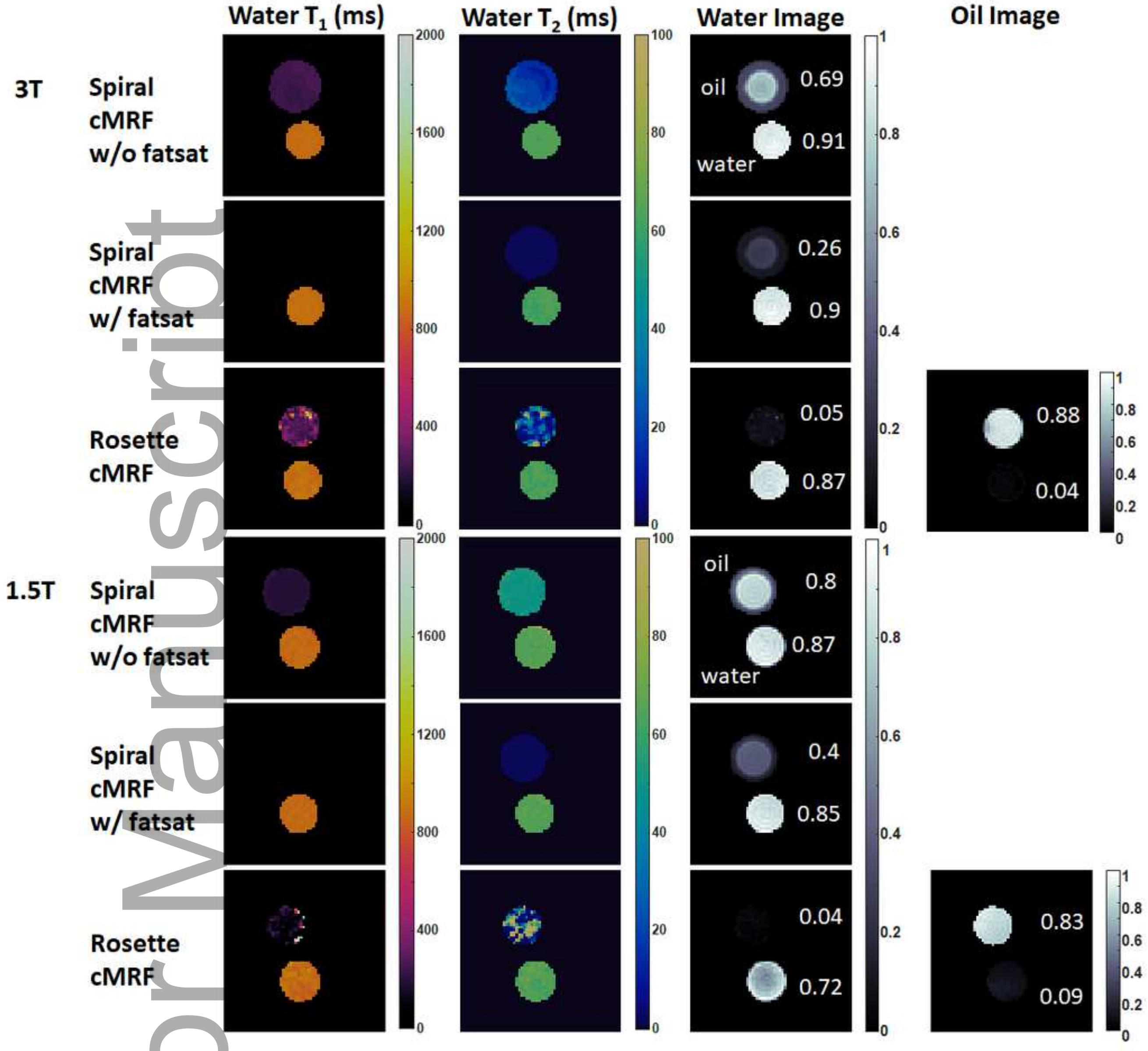

mrm_28404_f5.tif

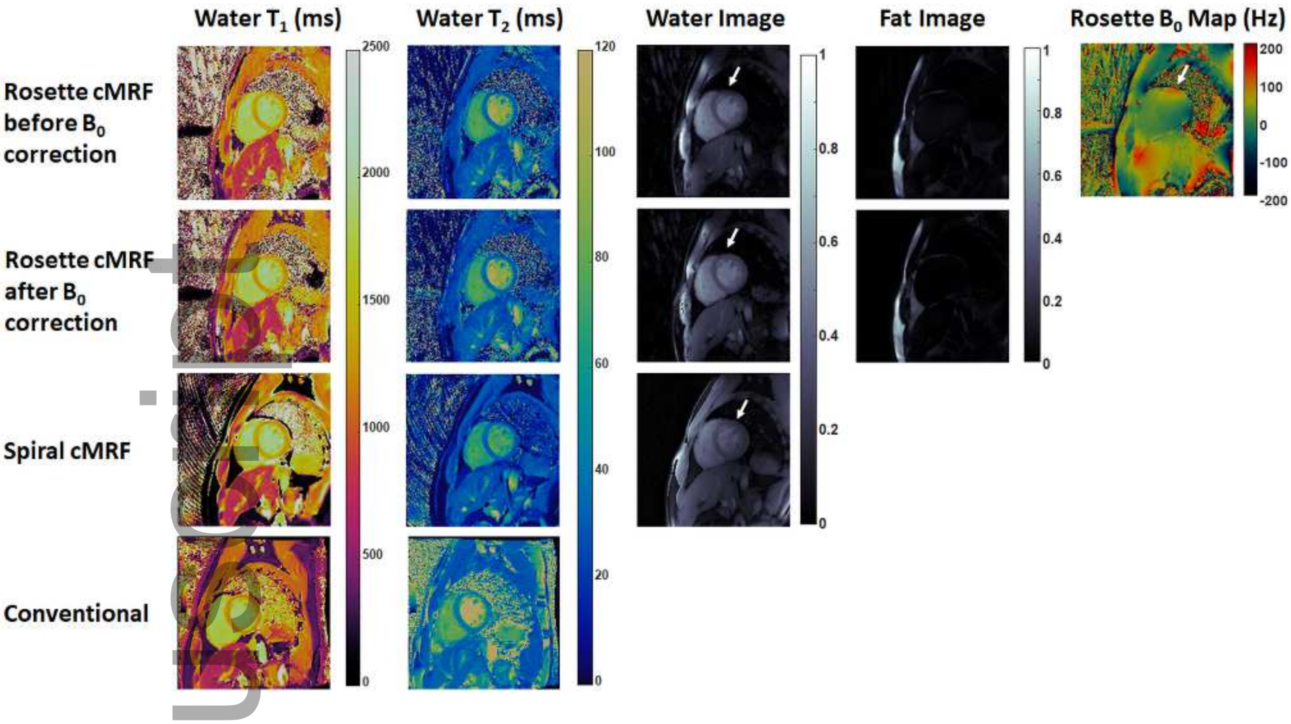

mrm_28404_f6.tif

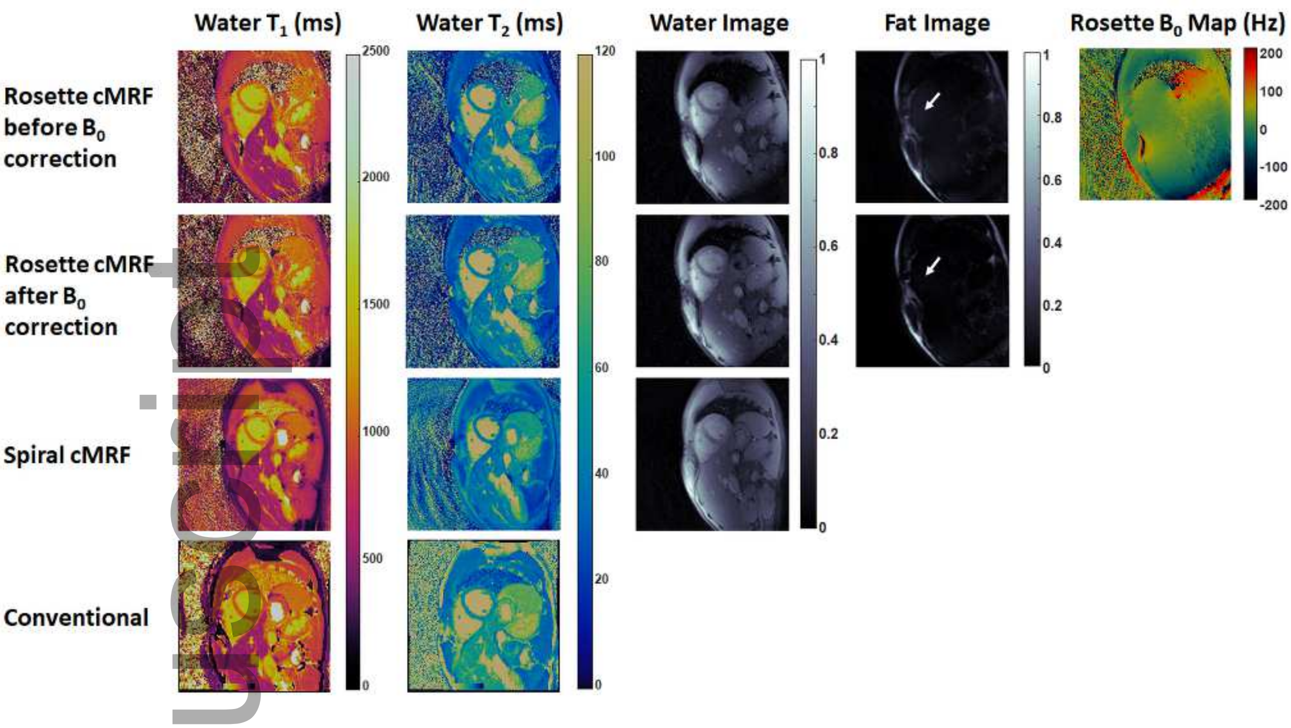

mrm_28404_f7.tif

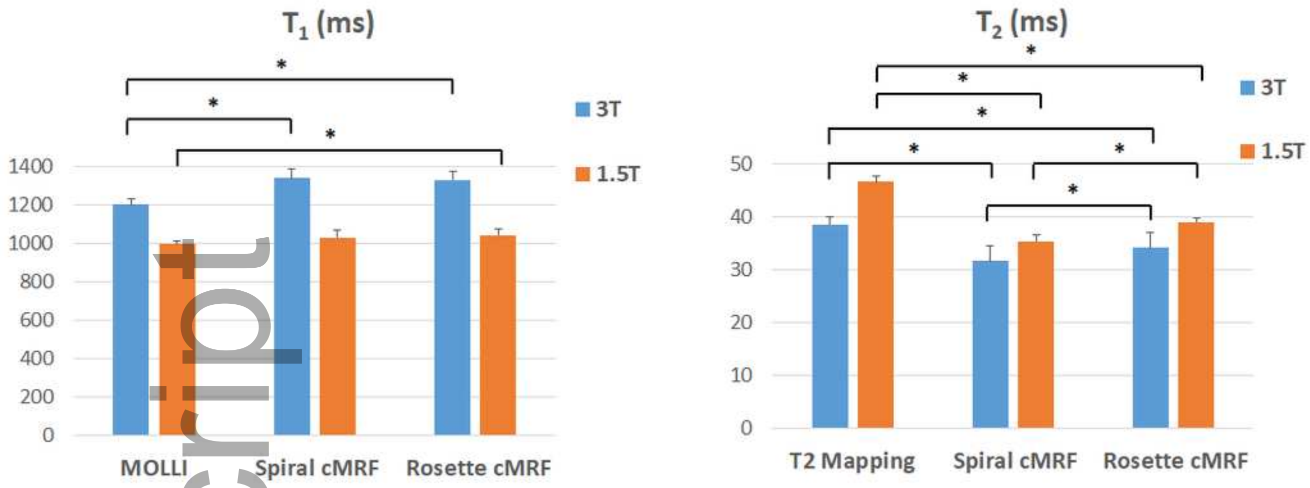

mrm_28404_f8.tif

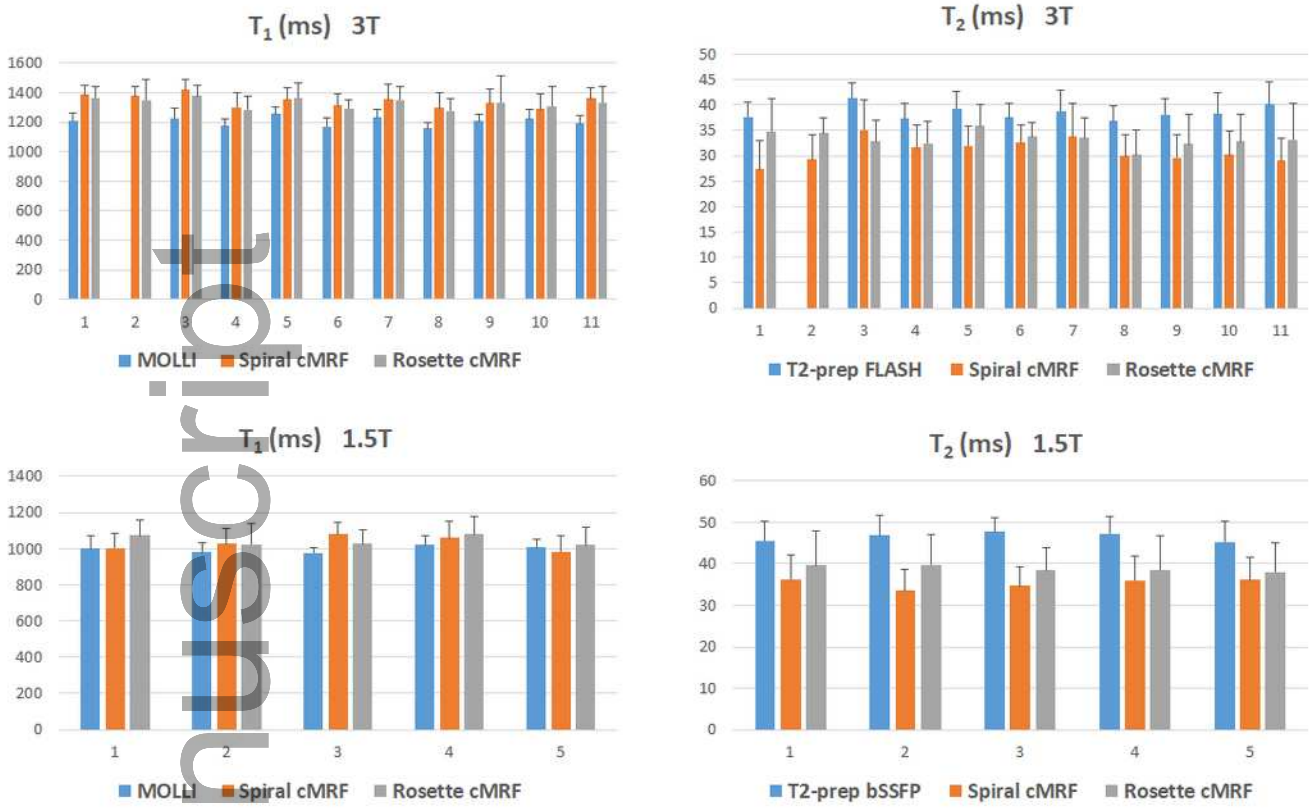

mrm_28404_f9.tif